# Multistatic bottom reverberation in shallow water

Henrik Schmidt, Jaiyong Lee, Huaiyu Fan, and Kevin LePage*

Department of Ocean Engineering
Massachusetts Institute of Technology
Cambridge, MA 02139
E-mail: henrik@keel.mit.edu

## Abstract

*A wavenumber integration approach to modeling of the full multistatic reverberant field produced by small-scale bottom roughness in stratified shallow water waveguides has been developed. A perturbation approach to rough elastic interface scattering has been combined with the OASES seismo-acoustic propagation model for stratified waveguides, yielding the capability of producing realizations and spatial statistics of bottom reverberation for multistatic sonar configurations in shallow water with a rough, stratified, elastic bottom. The formulation handles roughness with arbitrary anisotropic power spectra, and incorporates scattering into both the water column and the various seismic waves in the bottom.*

## 1. Introduction

A numerically efficient wave-theory model of the full multistatic reverberant field produced by small-scale roughness patches in stratified shallow water waveguides has been developed. A perturbation approach to rough elastic interface scattering [1, 2] has been combined with the OASES seismo-acoustic propagation model for stratified waveguides. The original perturbation theory was based on a 2-D Fourier transform formulation, allowing only short range reverberation modeling for computational reasons. However, coordinate transformations have been developed, translating the representation for the scattered field into an azimuthal Fourier series expansion of wavenumber integrals. This representation is directly compatible with the 3-D version of the OASES/SAFARI code [3], which has consequently been modified to provide extremely efficient numerical simulation of high-frequency seismo-acoustic reverberation in shallow water waveguides. The model's efficiency allows for Monte-Carlo estimation of the statistical properties of the reverberation from patches with anisotropic roughness statistics, including mean reverberation intensity and spatial correlation.

## 2. Rough Interface Reverberation Theory

### 2.1. Perturbation Theory

The perturbation theory for scattering from rough elastic interfaces decomposes the wavefield into coherent and scattered components of the field potentials in layer number $\ell$,

$$\chi_\ell = \langle \chi_\ell \rangle + s_\ell = \begin{cases} \phi_\ell &= \langle \phi_\ell \rangle + p_\ell \\ \psi_\ell &= \langle \psi_\ell \rangle + q_\ell \\ \Lambda_\ell &= \langle \Lambda_\ell \rangle + r_\ell \end{cases} \tag{1}$$

where $\chi_\ell$ is a generic potential representing the compressional potential $\phi_\ell$ and the two scalar shear potentials $\psi_\ell$ and $\Lambda_\ell$, representing SH and SV waves, respectively [3].

Away from physical sources and the rough interfaces, both the coherent and scattered potentials satisfy homogeneous Helmholtz equations

$$\left[\nabla^2 + k_\ell^2\right] \langle \chi_\ell(\vec{\mathbf{x}}) \rangle = 0 , \tag{2}$$

$$\left[\nabla^2 + k_\ell^2\right] s_\ell(\vec{\mathbf{x}}) = 0 , \tag{3}$$

*Presently with BBN Systems and Technologies, Cambridge, MA 02138.

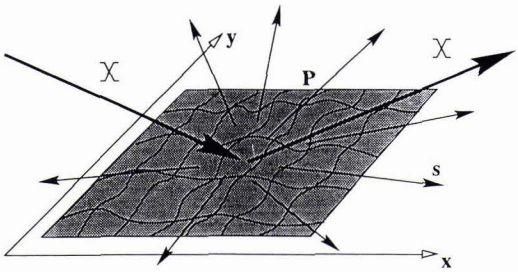


Figure 1: Rough interface patch in stratified waveguide, insonified by a seismo-acoustic field.

where $k$ represents the appropriate medium wavenumbers.

In addition, the fields must satisfy the boundary conditions at all interfaces $z_\ell$ in the stratification, as well as the source conditions. Assuming the *physical sources* are limited to a single depth, $z_s$, a dummy interface is added at this depth, and the interface conditions may be written in the operator form

$$B_\ell(\vec{\mathbf{x}})\langle\chi_{\ell;\ell+1}(\vec{\mathbf{x}})\rangle = -f_s(\vec{\mathbf{x}})\delta(z_\ell - z_s)\ , \ell = 1, 2\cdots N\ . \tag{4}$$

where N is the total number of physical and dummy interfaces in the stratification. The differential matrix operator $B_\ell$ represents the derivatives relating the physical parameters involved in the boundary conditions to the potentials [1]. Thus, Eq. 4 represents continuity conditions at all physical interfaces and discontinuity conditions imposed by the physical source distribution $f_s(\vec{\mathbf{x}})$.

Similarly, the perturbation theory leads to a set of boundary conditions to be satisfied by the scattered field $s(\vec{\mathbf{x}})$ at all interfaces in the stratification [2], including a rough interface at depth $z_v$,

$$B_\ell(\vec{\mathbf{x}})s_{\ell;\ell+1}(\vec{\mathbf{x}}) = -f_v(\vec{\mathbf{x}})\delta(z_\ell - z_v)\ , \ell = 1, 2\cdots N \tag{5}$$

where the distribution function $f_v(\vec{\mathbf{x}})$ is given by [1, 4, 5]

$$f_v(\vec{\mathbf{x}}) = \left[\overbrace{\gamma(\vec{\mathbf{x}})\frac{\partial B_\ell(\vec{\mathbf{x}})}{\partial z}}^{\text{elevation}} + \overbrace{\nabla\gamma(\vec{\mathbf{x}})\circ b_\ell(\vec{\mathbf{x}})}^{\text{rotation}}\right]\langle\chi_{\ell;\ell+1}(\vec{\mathbf{x}})\rangle\ . \tag{6}$$

Here, $\gamma(\vec{\mathbf{x}})$ is the interface roughness elevation. $B_\ell$ is the same boundary operator as above, while $b_\ell$ represents the rotation of the boundary conditions due to the roughness slope.

Obviously, Eq. 5 is totally equivalent to Eq. 4, with the physical source distribution $f_s(\vec{\mathbf{x}})$ replaced by the distribution function $f_v(\vec{\mathbf{x}})$ at the depth of of the rough interface. Thus, $f_v(\vec{\mathbf{x}})$ represents a *virtual source distribution*, the amplitude and phase distributions of which are determined by the coherent field and the roughness through Eq. 6.

### 2.2. Wavenumber Representation

For interfaces corresponding to separable cartesian geometry, the boundary equations 4 and 5 are conveniently transformed into the wavenumber domain, yielding for the scattered field [2]

$$\widetilde{s}^{\mp}_{\ell;\ell+1}(\vec{\mathbf{q}}) = -\widetilde{B}^{-1}_\ell(\vec{\mathbf{q}})\frac{1}{2\pi}\int d^2\vec{\mathbf{k}}\widetilde{\gamma}(\vec{\mathbf{q}}-\vec{\mathbf{k}})\left[\frac{\partial\widetilde{B}_\ell(\vec{\mathbf{k}})}{\partial z} - j(\vec{\mathbf{q}}-\vec{\mathbf{k}})\widetilde{b}_\ell(\vec{\mathbf{k}})\right]\langle\widetilde{\chi}^{\mp}_{\ell;\ell+1}(\vec{\mathbf{k}})\rangle \tag{7}$$

For random, spatially homogeneous interface roughness, the roughness statistics is given by the spatial correlation function $N_\ell(\Delta\vec{\mathbf{r}})$ or its Fourier transform, the normalized roughness power spectrum $P_\ell(\vec{\mathbf{p}})$, and the roughness variance $\langle\gamma^2_\ell\rangle$

$$N_\ell(\Delta\vec{\mathbf{r}}) = \langle\gamma_\ell(\vec{\mathbf{r}})\gamma_\ell(\vec{\mathbf{r}}+\Delta\vec{\mathbf{r}})\rangle \tag{8}$$

$$\langle\gamma^2_\ell\rangle P_\ell(\vec{\mathbf{p}}) = \frac{1}{2\pi}\int d^2\Delta\vec{\mathbf{r}}N_\ell(\Delta\vec{\mathbf{r}})e^{-j\vec{\mathbf{p}}\cdot\Delta\vec{\mathbf{r}}} \tag{9}$$

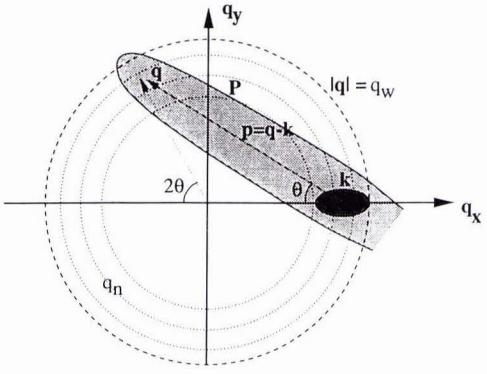


Figure 2: Graphical representation of the scattering wavenumber kernel. The scattered field is a convolution in the wavenumber plane of the incident field by the anisotropic roughness wavenumber spectrum.

Then, the following expression is achieved for the spatial correlation function for the scattered field [2]

$$C_S(\vec{\mathbf{r}}_1, z_1, \vec{\mathbf{r}}_2, z_2) = \frac{\langle \gamma_\ell^2 \rangle}{(2\pi)^3} \int d^2\vec{\mathbf{p}} P_\ell(\vec{\mathbf{p}}) \left[ \int d^2\vec{\mathbf{q}} A_m(z_1, \vec{\mathbf{q}}, \vec{\mathbf{q}} + \vec{\mathbf{p}}) e^{-j\vec{\mathbf{q}}\cdot\vec{\mathbf{r}}_1} \right] \left[ \int d^2\vec{\mathbf{q}} A_n(z_2, \vec{\mathbf{q}}, \vec{\mathbf{q}} + \vec{\mathbf{p}}) e^{-j\vec{\mathbf{q}}\cdot\vec{\mathbf{r}}_2} \right]^\dagger \tag{10}$$

where $A_m(z, \vec{\mathbf{q}}, \vec{\mathbf{k}})$ is the scattering kernel

$$A_m(z, \vec{\mathbf{q}}, \vec{\mathbf{k}}) = e_m(z, \vec{\mathbf{q}}) \widetilde{T}^*_{\ell;m}(\vec{\mathbf{q}}, \vec{\mathbf{k}}) \langle \widetilde{\chi}^{\mp}_{\ell;\ell+1}(\vec{\mathbf{k}}) \rangle$$

Here $e_\ell(z, \vec{\mathbf{q}})$ contains the exponentials representing the up- and downgoing scattered wavefield in layer $\ell$, and $\widetilde{T}_{\ell;m}$ is a generalized *T-matrix* for the field in layer $m$ produced by scattering from rough interface number $\ell$,

$$\widetilde{T}_{\ell;m}(\vec{\mathbf{q}}, \vec{\mathbf{k}}) = -\widetilde{B}_\ell^{-1}(\vec{\mathbf{q}}) \frac{1}{2\pi} \left[ \frac{\partial \widetilde{B}_\ell(\vec{\mathbf{k}})}{\partial z} - j(\vec{\mathbf{q}} - \vec{\mathbf{k}}) \widetilde{b}_\ell(\vec{\mathbf{k}}) \right] \tag{11}$$

The scattering integrals of both Eq. (7) and (10) are of a form convolving a medium dependent boundary operator term by the roughness spectrum at the difference wavenumber. This *Bragg scattering* condition is illustrated graphically in Fig. 2. An incident field with a wavenumber spectrum centered around the wave vector $\vec{\mathbf{k}}$ is convolved with an anisotropic roughness spectrum with skewness $\theta$, creating a scattered field composed of wave vectors $\vec{\mathbf{q}}$ within the lightly shaded envelope in Fig. 2, representing the roughness spectrum. The medium dependent part of the kernel represents the modal structure of the waveguide, as indicated by the circles in Fig. 2. Thus, the resulting scattered field will have a modal structure in all directions, but shaded by the roughness spectrum centered at the incident wavenumber. As will be evident from the examples following below, the reverberation from finite size patches will qualitatively exhibit the same spectral behavior.

## 3. Finite Roughness Patch

Unfortunately, for realistic two-dimensionally rough interfaces, the convolution integrals in the correlation function, Eq. 10, become four-dimensional. Even though a normal-mode expansion of Eq. 10 has recently been developed, yielding orders of magnitude in computational savings [5], the full numerical evaluation of the three-dimensional field statistics through Eq. 10 has sofar been impossible. Consequently, numerical implementations have been limited to plane or axisymmetric problems with one-dimensional roughness [2, 5].

To allow modeling of the fully three-dimensional reverberant field important to multistatic sonar concepts, an alternative approach has therefore been developed. Instead of directly evaluating the spatial statistics through Eq. 10, a deterministic form of the perturbation theory has been developed, based on spatial integration over finite roughness patches. As described in the following, this formulation leads to field expressions which are evaluated using modified versions of existing seismo-acoustic propagation models. It yields extremely efficient computation of specific realizations of the reverberant field from rough interface patches, such that estimates of the 3-D spatial

field statistics can be readily achieved through Monte-Carlo simulation with random realizations of the roughness statistics.

For a finite size roughness patch or sonar footprint, the scattered field is more efficiently represented by spatial integral over the patch $P$,

$$s(\vec{\mathbf{x}}) = \int_P G_v(\vec{\mathbf{x}}, \vec{\mathbf{x}}_v) d^2\vec{\mathbf{x}}_v \tag{12}$$

where $G_v(\vec{\mathbf{x}}, \vec{\mathbf{x}}_v)$ is a *Generalized Green's Function* satisfying the standard Helmholtz equation, and the boundary conditions,

$$B_\ell(\vec{\mathbf{x}}) G_v(\vec{\mathbf{x}}, \vec{\mathbf{x}}_v) = -\delta(\vec{\mathbf{x}} - \vec{\mathbf{x}}_v) f_v(\vec{\mathbf{x}}) \delta(z_\ell - z_v) \; . \tag{13}$$

where the virtual source distribution $f_v(\vec{\mathbf{x}})$ is given by Eq. 6. In a horizontal stratification, Eq. 13 is most conveniently solved in the wavenumber domain,

$$\widetilde{B}_\ell(\vec{\mathbf{q}}) \widetilde{G}_v(\vec{\mathbf{q}}, \vec{\mathbf{x}}_v) = -\widetilde{f}_v(\vec{\mathbf{q}}, \vec{\mathbf{x}}_v) \delta(z_\ell - z_v) \; , \tag{14}$$

where the spectrum $\widetilde{f}_v(\vec{\mathbf{q}}, \vec{\mathbf{x}}_v)$ is the Fourier transform of the virtual 'point source' term $\delta(\vec{\mathbf{x}} - \vec{\mathbf{x}}_v) f_v(\vec{\mathbf{x}})$. It is a vector containing coherent displacement and stress discontinuities on the patch,

$$\widetilde{f}_v(\vec{\mathbf{q}}, \vec{\mathbf{x}}_v)^T \simeq \Delta \left[\widetilde{u}, \widetilde{v}, \widetilde{w}, \widetilde{\sigma}_{zz}, \widetilde{\sigma}_{zx}, \widetilde{\sigma}_{zy}\right] \tag{15}$$

The wavenumber spectrum of the total scattered field is then obtained by integrating the solutions to Eq. 14 over the patch,

$$\widetilde{s}(\vec{\mathbf{q}}) = \int_P \widetilde{G}_v(\vec{\mathbf{q}}, \vec{\mathbf{x}}_v) d^2\vec{\mathbf{x}}_v \; , \tag{16}$$

with the spatial distribution following by a two-dimensional Fourier synthesis,

$$s(\vec{\mathbf{x}}) = \frac{1}{2\pi} \int d^2\vec{\mathbf{q}} e^{-j\vec{\mathbf{q}}\cdot\vec{\mathbf{x}}} \left[ \int_P \widetilde{G}_v(\vec{\mathbf{q}}, \vec{\mathbf{x}}_v) d^2\vec{\mathbf{x}}_v \right] \tag{17}$$

When numerically evaluating the inverse Fourier transform, the wavenumber increments must satisfy the Nyquist criteria, $\Delta q_{x,y} \leq \pi / R_{\max}$ [6]. Unfortunately, this condition severely limits the maximum range $R_{\max}$ that is numerically feasible, to a few times the horizontal extent of the roughness patch [4].

However, it is possible to transform Eq. 14 to cylindrical coordinates, [7]. The associated spatial distribution of the field is then given by a Fourier series of Hankel transforms,

$$s(r, \theta) = \Sigma_m \left\{ \begin{array}{c} \cos m\theta \\ \sin m\theta \end{array} \right\} \int dq \; q J_m(rq) \left[ \int_P \widetilde{G}_v^m(q, r_v, \theta_v) r_v dr_v d\theta_v \right] \tag{18}$$

Here, the generalized Green's function $\widetilde{G}_v^m(q, r_v, \theta_v)$ can be directly computed using the three-dimensional version of OASES [3] with the virtual source distribution being the discontinuities of the displacement and stress components of $m$-th Fourier order on the patch,

$$\widetilde{f}_v^m(q, r_v, \theta_v)^T \simeq \Delta \left[\widetilde{u}^m + \widetilde{v}^m, \widetilde{u}^m - \widetilde{v}^m, \widetilde{w}^m, \widetilde{\sigma}_{zz}^m, \widetilde{\sigma}_{zr}^m + \widetilde{\sigma}_{z\theta}^m, \widetilde{\sigma}_{zr}^m - \widetilde{\sigma}_{z\theta}^m\right] \tag{19}$$

The details of the coordinate transformation relating the components of the cylindrical source terms $f_v^m$ in Eq. 19 with the cartesian components $f_v(\vec{\mathbf{q}}, \vec{\mathbf{x}}_v)$ in Eq. 15 involves a significant amount of algebra, the details of which are described in Ref.[7].

The Fourier series in Eq. 18 converges very fast for orders larger than the dimensionless size $ka$ of the patch, due to the asymptotic behavior of the virtual source terms

$$f_v^m(q, r_v, \theta_v) \sim J_m(qr_v) \to 0, \text{ for } m > qr_v \; , \tag{20}$$

and the truncation is therefore easily determined *a priori*. Thus, the number of significant terms in the series depends only on the patch size with the typical number being equal to a few times the *patch size* in wavelengths. In contrast the number of terms in the numerical evaluation of each of the two dimensions of the Fourier transform in Eq. 17 is determined by the *receiver range*. This difference is the key to the numerical superiority of the cylindrical form.

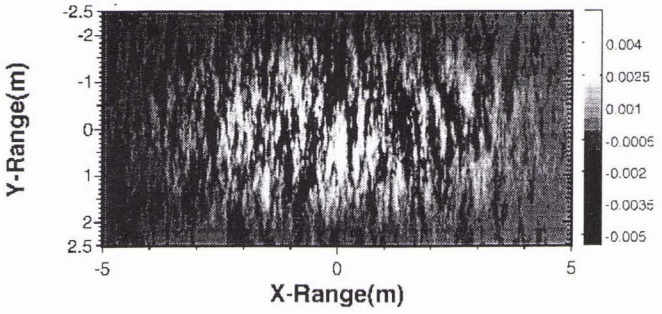


Figure 3: Bottom patch with anisotropic roughness, insonified from the left at 40 kHz. The roughness has a Goff-Jordan power spectrum with correlation lengths $l_x = 1.04$ m and $l_y = 0.13$ m, and RMS elevation of 4.7 mm.

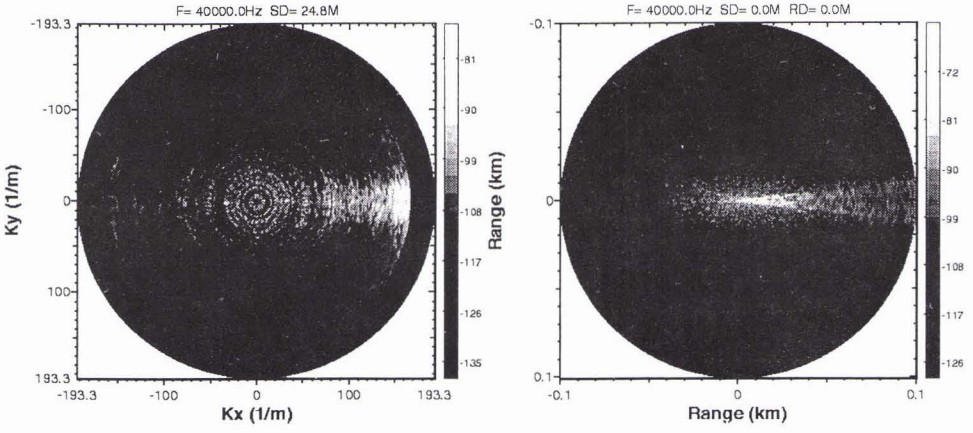


Figure 4: Multistatic reverberation from the roughness patch in Fig. 3. Left frame shows contours of the two-dimensional wavenumber spectrum of the scattered field 5.2 m above the seabed. The wavenumber of the incident field is $(k_x, k_y) = (168, 0)$ corresponding to incidence onto the patch from the left. The right frame shows contours of the scattered field in a horizontal plane at the same depth. Directions to the right represent forward scattering, while directions to the left represent backscattering.

## 4. Numerical Results

To illustrate the performance of the theoretical formulation in predicting the full multistatic reverberant field at high frequency, the Panama City bottom scattering experiment performed by Tang *et al.* is applied [8].

The experiment was carried out in a water depth of 30 m. An isovelocity water sound speed of 1495 m/s is assumed, and the bottom is assumed to be a homogeneous, elastic halfspace with compressional speed 1711 m/s, shear speed 118 m/s, and density 2.01 g/cm$^3$. The compression and shear attenuations were estimated to 0.09 dB/$\lambda$ and 0.2 dB/$\lambda$, respectively.

The bottom was insonified at low grazing angles by a 40 kHz projector mounted on a tower, 5.2 m above the bottom. The insonifying beam had a vertical and horizontal beamwidths of 6° and 14°, respectively. With a nominal grazing angle of 12.6° the sonar footprint was centered at a distance of 23 m from the tower, and had a size of approximately $10 \times 5$ m.

Figure 3 shows the sonar footprint with seabed roughness, for a case where the large main axis of the roughness power spectrum is aligned with the incident beam, i.e. the insonificition is 'broadside' to the roughness striation. The roughness has a Goff-Jordan [9] power spectrum with correlation lengths $l_x = 1.04$ m and $l_y = 0.13$ m, and RMS elevation of 4.7 mm.

Figure 4 shows the computed multistatic reverberation from the roughness patch in Fig. 3. Left frame shows

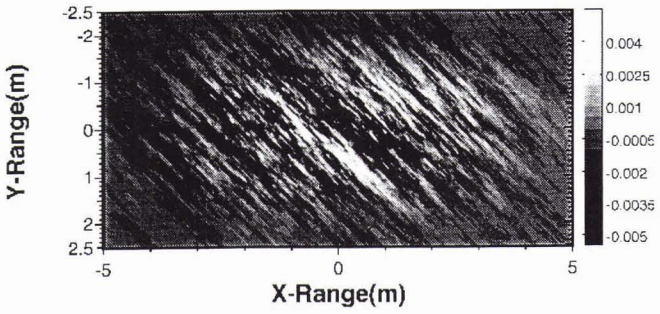


Figure 5: Bottom patch with anisotropic roughness, insonified from the left at 40 kHz. The roughness has a Goff-Jordan power spectrum with correlation lengths 1.04 m and 0.13 m, and RMS elevation of 4.7 mm. The skew angle of the roughness anisotropy is 45°

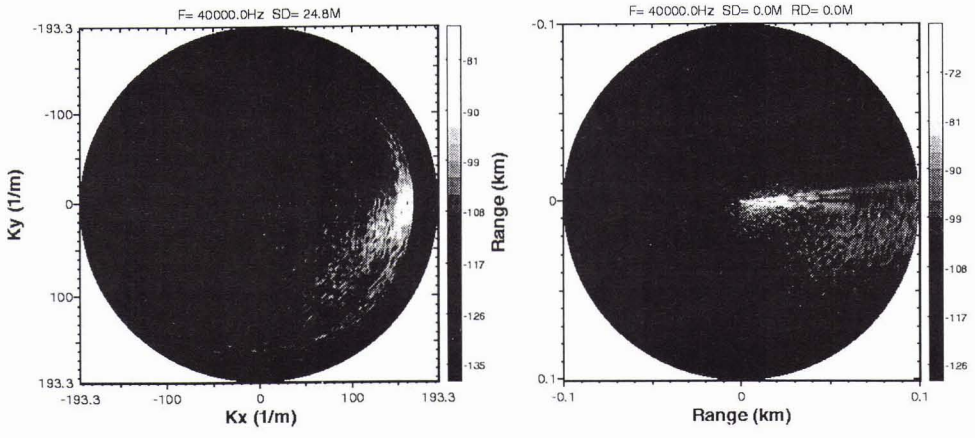


Figure 6: Multistatic reverberation from the roughness patch in Fig. 5. Left frame shows contours of the two-dimensional wavenumber spectrum of the scattered field 5.2 m above the seabed. The wavenumber of the incident field is $(k_x, k_y) = (168, 0)$ corresponding to incidence onto the patch from the left. The right frame shows contours of the scattered field in a horizontal plane at the same depth. Directions to the right represent forward scattering, while directions to the left represent backscattering.

contours of the two-dimensional wavenumber spectrum of the scattered field 5.2 m above the seabed. The wavenumber of the incident field is $(k_x, k_y) = (168, 0)$ corresponding to incidence onto the patch from the left. The right frame shows contours of the scattered field in the same horizontal plane, i.e. the same level as the projector. The square area shown is 200 × 200 m, centered over the sonar footprint. Directions to the right represent forward scattering, while directions to the left represent backscattering. In this 'broadside' configuration, even though the forward scattering is dominant, the backscattering is significant. On the other hand, the out-of-plane, i.e. ±90°, bistatic angles show very low reverberation levels.

Figure 5 shows the same sonar footprint, but with the main axes of the roughness anisotropy rotated counter-clockwise by 45° . The roughness statistics is the same as in the previous case, i.e. the power spectrum corresponds to correlation lengths 1.04 m and 0.13 m, and RMS elevation of 4.7 mm.

Figure 6 shows the computed multistatic reverberation from the roughness patch in Fig. 5. The left frame shows contours of the two-dimensional wavenumber spectrum of the scattered field 5.2 m above the seabed. Again the wavenumber of the incident field is $(k_x, k_y) = (168, 0)$ corresponding to incidence onto the patch from the left. The shading controlled by the Bragg scattering condition illustrated in Fig. 2 is evident, with the dominant scattering being into wave vectors in the lower right quadrant. This translates to out-of-plane-scattering towards the right relative to the incident direction, as is also evident in the right frame in Fig. 6 showing contours of the scattered field in the same horizontal plane. The square area shown is 200 × 200 m, centered over the sonar footprint. Again,

directions to the right represent forward scattering, while directions to the left represent backscattering. In this configuration the forward scattering is still dominant, but the monostatic backscatter is reduced substantially, replaced by a significant out-of-plane component. Consistent with Fig. 2, the dominant scattering spans angles up to 90° from the forward direction, corresponding to bistatic angles up to twice the roughness skew angle (45°) from the direction of the incident field.

## 5. Conclusion

A numerically efficient formulation for wave theory modeling of the full multistatic, reverberant field in stratified waveguides has been developed. A previously developed perturbation approach to scattering from rough interface patches has been transformed into a cylindrical coordinate formulation and implemented in the three-dimensional version of OASES/SAFARI. The new modeling capability has been applied to investigate the high-frequency reverberation from anisotropic roughness in a shallow water environment with a stratified, elastic bottom.

## Acknowledgements

This work was supported by the Office of Naval Research.

## References

[1] W.A. Kuperman and H. Schmidt. Self-consistent perturbation approach to rough surface scattering in stratified elastic media. *J. Acoust. Soc. Am.*, 86:1511–1522, 1989.

[2] H. Schmidt and W.A. Kuperman. Spectral representations of rough interface reverberation in stratified ocean waveguides. *J. Acoust. Soc. Am.*, 97(4):2199–2209, 1995.

[3] H. Schmidt and J. Glattetre. A fast field model for three-dimensional wave propagation in stratified environments based on the global matrix method. *J. Acoust. Soc. Am.*, 78:2105–2114, 1985.

[4] K. LePage. *Elastic scattering in oceanic waveguides.* PhD thesis, Massachusetts Institute of Technology, June 1992.

[5] B. Tracey and H. Schmidt. Seismo-acoustic field statistics in shallow water. *IEEE Journal of Oceanic Engineering*, Submitted, 1996.

[6] F. Jensen, W.A. Kuperman, M.B. Porter, and H. Schmidt. *Computational Ocean Acoustics.* AIP Press, New York, 1994.

[7] H. Fan. *Wave theory modeling of three-dimensional seismo-acoustic reverberation in ocean waveguides.* PhD thesis, Massachusetts Institute of Technology, September 1995.

[8] D.J. Tang, G. Jin, D.R. Jackson, and K.L. Williams. Analyses of high-frequency bottom and subbottom backscattering for two distinct shallow water environments. *J. Acoust. Soc. Am.*, 96:2930–2936, 1994.

[9] J. Goff and T. Jordan. Stochastic modeling of seafloor morphology: Inversion of sea beam data for second order statistics. *J. Geophys. Res.*, 93:13589–13608, 1988.